



RESEARCH ARTICLE | SEPTEMBER 06 2023

## Effect of acoustic metasurface on hypersonic-boundary-layer wave packet

Peixu Guo (郭培旭) ; Xiao Liu (刘潇) ; Rui Zhao (赵瑞)  ; Jiaao Hao (郝佳傲) ; Chih-Yung Wen (温志湧) 



*Physics of Fluids* 35, 094110 (2023)

<https://doi.org/10.1063/5.0168193>



View  
Online



Export  
Citation

### Articles You May Be Interested In

Design of broadband time-domain impedance boundary conditions using the oscillatory-diffusive representation of acoustical models

*J. Acoust. Soc. Am.* (September 2016)

Time-domain impedance boundary condition modeling with the discontinuous Galerkin method for room acoustics simulations

*J. Acoust. Soc. Am.* (April 2020)

Linear stability analysis of second-mode attenuation via porous carbon-matrix ceramics

*Physics of Fluids* (June 2023)



Physics of Fluids

Special Topics Open  
for Submissions

[Learn More](#)

# Effect of acoustic metasurface on hypersonic-boundary-layer wave packet

Cite as: Phys. Fluids **35**, 094110 (2023); doi: [10.1063/5.0168193](https://doi.org/10.1063/5.0168193)

Submitted: 18 July 2023 · Accepted: 23 August 2023 ·

Published Online: 6 September 2023



Peixu Guo (郭培旭),<sup>1,a)</sup> Xiao Liu (刘潇),<sup>2</sup> Rui Zhao (赵瑞),<sup>2,b)</sup> Jiaao Hao (郝佳傲),<sup>1</sup>   
and Chih-Yung Wen (温志湧)<sup>1</sup>

## AFFILIATIONS

<sup>1</sup>The Hong Kong Polytechnic University, Kowloon, Hong Kong

<sup>2</sup>Beijing Institute of Technology, Beijing 100081, People's Republic of China

<sup>a)</sup>Electronic mail: [peixu.guo@outlook.com](mailto:peixu.guo@outlook.com)

<sup>b)</sup>Author to whom correspondence should be addressed: [zr@bit.edu.cn](mailto:zr@bit.edu.cn)

## ABSTRACT

Effect of the acoustic metasurface on a broadband wave packet in a Mach 6 boundary layer is studied. Direct numerical simulations (DNSs) with time-domain impedance boundary condition (TDIBC) and metasurface with microstructures are performed. It is shown that DNS with TDIBC resolves the amplitude and phase information of the wave packet satisfactorily. The minor prediction discrepancy arises from the modeling error in the acoustic impedance. The interesting finding of this paper is that the metasurface behaves as an equivalent unsteady blowing-suction model to perturb the wall-normal velocity and then passively the pressure field. Although both pressure and wall-normal velocity appear in the characteristic-wave variable, the pressure can be decoupled to be updated by the Neumann condition, as usually employed in Navier–Stokes solvers. The dominant frequency scale that enables reproducing the stabilization effect of the metasurface is found to be slightly smaller than the energetic frequency maximum of the wave packet. This observation indicates that the high-frequency unsteadiness nature of the blowing-suction behavior is indispensable, which is induced by the interaction of the metasurface and the wave packet. For the stabilization mechanism, energy analysis reveals that a dilatation-related work near the wall is significantly suppressed by the metasurface, which agrees with the wall-normal location where the wave-packet fluctuation gets attenuated.

Published under an exclusive license by AIP Publishing. <https://doi.org/10.1063/5.0168193>

## I. INTRODUCTION

Laminar to turbulent transition in hypersonic boundary layers is intensively concerned due to its significance in the design of re-entry or air-breathing vehicles.<sup>1,2</sup> Due to the light freestream turbulence intensity in a flight environment, natural transition induced by a small-amplitude eigenmode is the most possible scenario. For two-dimensional (2D) configurations with minor or no curvature, the first-mode oblique wave is linearly the most unstable one in supersonic states below around Mach number 4, while the second-mode planar wave of acoustic nature is dominant otherwise under hypersonic conditions.<sup>3</sup> To delay the transition mostly caused by the second mode, active<sup>4,5</sup> or passive<sup>6–8</sup> control techniques have been proposed. The active control is currently difficult to be applied due to severe aerodynamic and aerothermal surface environment and high requirement for energy input. Therefore, passive strategy seems more promising in engineering applications, such as an acoustic metasurface implemented by a porous coating.<sup>9–11</sup> The acoustically absorptive porous wall was found to effectively stabilize the second mode,<sup>12</sup> which was

confirmed experimentally.<sup>13</sup> For the low-frequency first mode, however, the porous wall was found to marginally destabilize it,<sup>14</sup> and the degree of destabilization was associated with the phase of the wall acoustic admittance.<sup>15,16</sup> In reality, in response to freestream turbulence with continuous spectra, the boundary layer disturbances possess a wide frequency range, covering components with and without the acoustic property. How an acoustic metasurface interacts with a broadband disturbance is of further interest in the present paper.

For pre-transitional flows mainly in the linear instability regime, direct numerical simulation (DNS) requires evidently less computational cost than for fully developed turbulent flows and hardly introduces modeling assumptions. With regard to a single-frequency disturbance, the acoustic impedance boundary condition can be straightforwardly transformed into the time domain and efficiently coupled with a Navier–Stokes (N–S) solver. Thus, meshing the microcavities in the metasurface is conveniently replaced by an embedded boundary condition. A spatial DNS, which is preferred in the convective instability problem, can be simply performed in the time

domain.<sup>17</sup> For broadband disturbances with a frequency-dependent impedance, Fund and Ju<sup>18</sup> established an elegant formulation of the time-domain impedance boundary condition (TDIBC) to avoid repeated Fourier transforms and save computational cost. In-depth numerical considerations and discussions are included in Refs. 19–22. These characteristic boundary conditions have been applied in high-fidelity simulations of wall-bounded turbulent flows,<sup>23,24</sup> flows in thermoacoustic engines,<sup>25</sup> and the stability of the second mode<sup>26,27</sup> with the presence of porous walls.

This paper aims to elaborate the underlying mechanism on the interaction between the acoustic metasurface and the 2D broadband wave packet through the convenient tool TDIBC. It has been known that the stabilization effect of the acoustic metasurface can be well modeled by the relation  $\hat{p}(\omega) = -Z(\omega) \hat{v}(\omega)$ , where  $\hat{p}$  and  $\hat{v}$  are Fourier transform of the wall fluctuations of pressure and wall-normal velocity, and  $Z$  is the frequency-dependent specific impedance. Currently, linear stability and sensitivity analyses can be used to predict the instability evolution and the response to the presence of wall impedance.<sup>28–32</sup> In this paper, we proceed from “predicting” or “calculating” toward “understanding” the effect of the metasurface by examining how the fluctuations  $p'$  and  $v'$  interplay to reduce the fluctuations in a broadband wave packet. It merits investigations on to what degree  $p'$  and  $v'$  can be decoupled and what the dominant frequency band (or timescale) is in stabilizing the broadband wave packet. In this study, we perform thought experiments based on DNS with conventional and modified TDIBCs. If different TDIBC models report similar performance, the modification or simplification of the model can be furthered until the dominant physical effect is identified. Details of the modified TDIBC (MTDIBC) will be introduced later. Another point to be addressed is the effect of the metasurface on the amplification of the wave packet from an energy perspective. Previous similar studies concentrate on the single-frequency disturbances,<sup>33,34</sup> whereas the investigation on the more realistic wave packet is in lack. If the disturbance is in the form of wave packets, the analysis is expected to approach the real-life instability or transition scenario better than those initiated by single-frequency disturbances. The present study may facilitate a deeper understanding of the role of the metasurface in the stability and transition control.

Before addressing the physical aspect, an identification of the origin of the prediction discrepancy between the TDIBC and the

metasurface is needed first. It remains unclear whether and to what degree the error arises from the numerical aspect in TDIBC implementation, the acoustic impedance modeling or the cavity-induced base-flow distortion effect. Comparative studies are performed between the TDIBC and an acoustic metasurface case with meshed micro-cavities. The flow past and inside the microstructures of the acoustic metasurface is fully resolved. The article is organized as follows. The considered physical problem, methodology, and computational setup are introduced in Sec. II. The analysis of the prediction discrepancy is conducted first and the physical effects of the metasurface on the boundary layer disturbances are discussed then in Sec. III. Concluding remarks are shown in Sec. IV.

## II. PROBLEM FORMULATION AND SIMULATION STRATEGY

As shown by Fig. 1, a Mach 6 2D flat-plate boundary layer with a sharp leading edge is directly simulated. Cartesian co-ordinates are constructed with the origin at the leading edge, and  $x$  and  $y$  denote the streamwise and wall-normal directions, respectively. The free-stream conditions, identical to the wind tunnel ones by Bountin *et al.*,<sup>35</sup> are given as follows: Mach number  $Ma_\infty = 6.0$ , static temperature  $T_\infty^* = 43.18$  K, and unit Reynolds number  $Re_{1\infty}^* = 1.05 \times 10^7 \text{ m}^{-1}$ , where the asterisk denotes the dimensional quantity. The wall is assumed to be isothermal with a temperature of  $T_w^* = 293$  K, where the subscript “w” represents the quantity on the wall. In addition, a no-slip velocity boundary condition is given on the wall boundary, and a no-penetration condition is imposed except for the blowing-suction strip and impedance boundaries. A perfect gas assumption is made with the specific heat ratio being  $\gamma = 1.4$ . The Prandtl number is assumed to be  $Pr = 0.72$ , and the dynamic viscosity is computed by the Sutherland’s law. The primitive variables are non-dimensionalized by the corresponding freestream base-flow quantities, except that the pressure  $p$  is by  $\rho_\infty u_\infty^2$ , where  $\rho$  and  $u$  are the density and streamwise velocity, respectively. The reference length scale  $L_{\text{ref}}^* = 0.2$  m is used for non-dimensionalization. A single-frequency or Gaussian broadband disturbance is introduced through the wall blowing-suction technique between  $x_1 = 0.0523$  and  $x_2 = 0.0773$  in Fig. 1. The surface wall-normal momentum density is disturbed, whose dimensionless form is given by

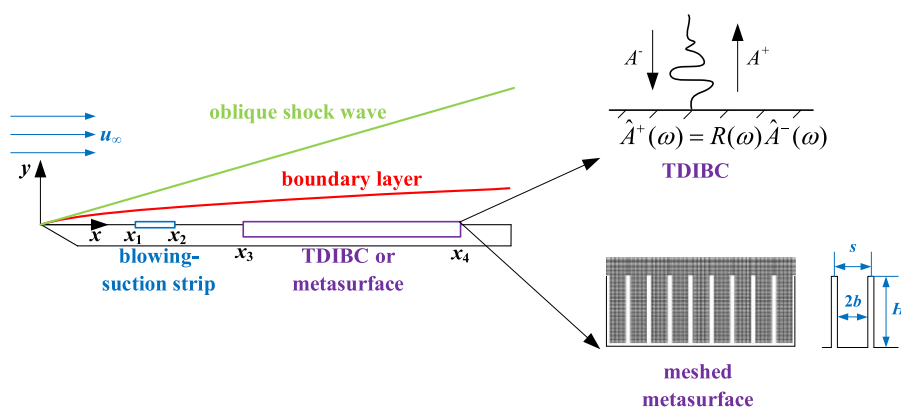


FIG. 1. Schematic drawing of the physical problem.

$$(\rho v)'_w(x, t) = \begin{cases} \epsilon \sin\left(2\pi \frac{x - x_1}{x_2 - x_1}\right) \sin(\omega t), \\ \text{for single-frequency disturbance,} \\ \epsilon \sin\left(2\pi \frac{x - x_h}{x_2 - x_1}\right) \exp\left\{-\frac{(t - t_a - [t/T]T)^2}{2\sigma_b^2}\right\}, \\ \text{for broadband disturbance.} \end{cases} \quad (1)$$

Here, the amplitude  $\epsilon = 0.001$  is given, and  $t$  denotes time. For the single-frequency case, the angular frequency is  $\omega = 220.6$  and the dimensional frequency is  $f^* = 138.74$  kHz, which finally evolve into a second mode in around  $x > 0.5$ .<sup>36</sup> For the broadband disturbance case in Eq. (1), the parameters are given by  $x_h = (x_1 + x_2)/2$ ,  $t_a = 0.0119$ ,  $T = 1.6$ , and  $\sigma_b = 0.0016$ . Furthermore, the operator “[.]” in Eq. (1) represents a floor function, i.e., the greatest integer function. Thus, the broadband disturbance is generated in the form of a pulse wavepacket with a period of  $T = 1.6$ . The spectra of the broadband mass-flow pulse in the blowing-suction strip and the response of the pressure right downstream are shown in Fig. 2. Throughout this paper, fast Fourier transform (FFT) is performed to obtain spectra of signals after taking sampling every 100 time steps during a period of the broadband pulse, which corresponds to a dimensional sampling frequency of 1.98 MHz.

Downstream of the forcing region in Fig. 1, a TDIBC or an acoustic metasurface beneath the boundary layer with subwavelength grooves (2D cavities) is imposed between  $x_3$  and  $x_4$ , where  $x_3 = 0.2$  and  $x_4 = 1$ . Sponge zones are placed in the range  $x > 1$  to minimize the reflection of disturbances near the outflow boundary. In the schematic drawing of the TDIBC,  $A^+$  and  $A^-$  represent the up-traveling reflection and down-traveling incident characteristic waves, respectively, and  $R$  is the reflection coefficient to be modeled. With regard to the metasurface case, the dimensionless half width  $b = 9.8 \times 10^{-4}$ , the unit-cell period  $s = 2.6 \times 10^{-3}$ , and depth  $H = 8.21 \times 10^{-3}$  are identical to those in Ref. 17, as shown in Fig. 1. The geometric setting corresponds to a porosity of  $\phi = 2b/s \approx 0.75$ . The model of the wall

admittance or impedance has recently been improved by the authors<sup>37</sup> to include the effect of high-order diffracted modes inside the microstructure. The dimensionless specific impedance  $Z = -\hat{p}(\omega)/\hat{v}(\omega)$  on the bottom wall is calculated based on that model.

The 2D compressible N-S equation for DNS can be expressed in the dimensionless conservative form in the Cartesian co-ordinate system:

$$\frac{\partial}{\partial t} \mathbf{U} + \frac{\partial}{\partial x} \mathbf{F}_1 + \frac{\partial}{\partial y} \mathbf{F}_2 = 0, \quad (2)$$

where

$$\begin{cases} \mathbf{U} = (\rho, \rho u, \rho v, E)^T, \\ \mathbf{F}_1 = (\rho u, \rho u^2 + p - \sigma_{xx}/Re_\infty, \rho uv - \sigma_{xy}/Re_\infty, u(E + p) \\ \quad - (u\sigma_{xx} + v\sigma_{xy} - q_x)/Re_\infty)^T, \\ \mathbf{F}_2 = (\rho v, \rho uv - \sigma_{xy}/Re_\infty, \rho v^2 + p - \sigma_{yy}/Re_\infty, v(E + p) \\ \quad - (u\sigma_{xy} + v\sigma_{yy} - q_y)/Re_\infty)^T. \end{cases} \quad (3)$$

Here, the Reynolds number based on the reference scale is calculated to be  $Re_\infty = 2.1 \times 10^6$ , and the total energy per unit volume reads

$$E = \frac{p}{\gamma - 1} + \rho \frac{u^2 + v^2}{2}. \quad (4)$$

Under the Stoke's hypothesis for the bulk viscosity, the components of the stress tensor and heat flux are expressed by

$$\begin{aligned} \sigma_{xx} &= 2\mu \frac{\partial u}{\partial x} - \frac{2}{3}\mu \left( \frac{\partial u}{\partial x} + \frac{\partial v}{\partial y} \right), \quad \sigma_{xy} = \sigma_{yx} = \mu \left( \frac{\partial u}{\partial y} + \frac{\partial v}{\partial x} \right), \\ \sigma_{yy} &= 2\mu \frac{\partial v}{\partial y} - \frac{2}{3}\mu \left( \frac{\partial u}{\partial x} + \frac{\partial v}{\partial y} \right), \\ q_x &= -\frac{\mu}{(\gamma - 1)PrMa_\infty^2} \frac{\partial T}{\partial x}, \quad q_y = -\frac{\mu}{(\gamma - 1)PrMa_\infty^2} \frac{\partial T}{\partial y}. \end{aligned} \quad (5)$$

The Prandtl number is assumed to be  $Pr = 0.72$ , and the dynamic viscosity is computed by the Sutherland's law  $\mu = T^{3/2}(T_r^*/T_\infty^* + 1)/(T_r^*/T_\infty^* + T)$ , where  $T_r^* = 110.4$  K. Equation (2) is finally transformed into the generalized curvilinear co-ordinate system and solved.

DNS is performed based on the high-order accurate finite difference method.<sup>36</sup> For all the cases considered, the fifth-order upwind compact scheme is used to discretize the inviscid term, and the sixth-order central difference scheme is applied to discretize the viscous term. The three-stage third-order total variation diminishing (TVD) Runge-Kutta method is employed for time marching. Under the same flow, geometric, and mesh conditions, previous studies of the authors have fully validated the solver and convergence of the mesh resolution and time step size.<sup>17,36</sup> Specifically, the computational mesh above  $y = 0$  possesses  $1607 \times 200$  nodes, clustering near the leading edge and the wall boundary. Inside each cavity,  $12 \times 83$  nodes are sufficient for the convergence of the stationary flow.<sup>17</sup> The time step size is set to  $\Delta t = 2 \times 10^{-5}$ , which corresponds to a dimensional frequency of  $\Delta f^* \approx 197.58$  MHz. Dirichlet conditions are enforced for the stream-wise velocity and temperature on the wall, i.e.,  $u = 0$  and  $T = T_w$ . In terms of the wall-normal velocity and pressure, the boundary conditions are introduced below.

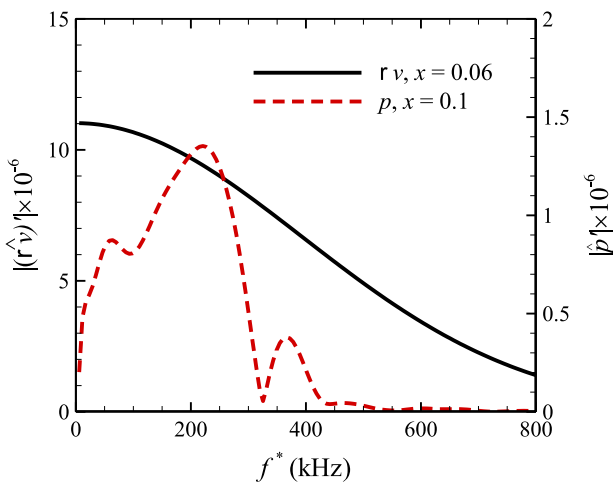


FIG. 2. Spectra of the wall-normal mass flow rate at  $x = 0.06$  in the blowing-suction strip and of the pressure at  $x = 0.1$  downstream.

### A. Direct coupling method for a constant impedance

For a single-frequency disturbance, the wall specific acoustic impedance can be approximated as a constant  $Z_0$  that does not vary with the frequency. The fluctuations are also assumed to possess exponential time dependence, i.e., proportional to  $e^{-i\omega t}$ . Consequently, the impedance is straightforwardly coupled with the N-S solver by taking the real part of  $\hat{p}(\omega) = -Z_0 \hat{v}(\omega)$  on the bottom wall boundary as follows:

$$v(t) = -\text{Re}\left(\frac{1}{Z_0}\right)p(t) + \text{Im}\left(\frac{1}{Z_0}\right)\frac{dp(t)}{\omega dt}, \quad (6)$$

where  $\text{Re}(\cdot)$  and  $\text{Im}(\cdot)$  represent taking the real and imaginary parts, respectively. The above-mentioned equation prescribes the boundary condition for the wall-normal velocity, while the pressure on the wall is obtained via the approximation  $dp/dy = 0$ . This approach has been confirmed to be accurate by our previous work.<sup>17</sup>

### B. Time-domain impedance boundary conditions (TDIBC)

For problems with frequency-dependent impedance, classical formulation of TDIBC by Fung and Ju<sup>18</sup> is introduced in the present paper. Given the renormalized pressure fluctuation  $p'_a = p' / (\bar{\rho}_w \bar{a}_w)$ , where  $a$  is the sound speed, the amplitude of the up-traveling reflection and down-traveling incident characteristic waves are given by

$$A^+ = v' + p'_a, \quad A^- = v' - p'_a, \quad (7)$$

respectively. The two waves are causally correlated by the reflection coefficient in the frequency domain as  $\hat{A}^+(\omega) = R(\omega)\hat{A}^-(\omega)$ . Based on the specific impedance  $Z_a = -\hat{p}_a(\omega)/\hat{v}(\omega)$  via the model in Ref. 37, the reflection coefficient is computed by  $R(\omega) = (1 - Z_a)/(1 + Z_a)$ . The wall softness  $W$  is then obtained as  $W(\omega) = 1 + R(\omega) = 2/(1 + Z_a)$ . Accordingly, it yields

$$\hat{A}^+(\omega) = -\hat{A}^-(\omega) + W(\omega)\hat{A}^-(\omega). \quad (8)$$

Fung and Ju<sup>18</sup> proposed to approximate the softness by a multi-oscillator model:

$$W(\omega) \approx \sum_{k=1}^{n_k} \left( \frac{\beta_k}{i\omega - p_k} + \frac{\beta_k^*}{i\omega - p_k^*} \right), \quad (9)$$

where  $(p_k, \beta_k)$  represent the pole and residue, the superscript <sup>\*</sup> denotes complex conjugate, and  $n_k$  is the total number of conjugate pairs. By applying the Laplace transform and assuming  $\text{Re}(p_k) < 0$ , Eq. (8) is transformed into the time domain at the instant  $t + \Delta t$ ,

$$A^+(t + \Delta t) = -A^-(t + \Delta t) + \sum_{k=1}^{n_k} G_k^-(t + \Delta t) + \text{c.c.}, \quad (10)$$

where

$$G_k^-(t + \Delta t) = \int_0^\infty \beta_k e^{p_k \tau} A^-(t + \Delta t - \tau) d\tau, \quad (11)$$

and c.c. denotes complex conjugate. The above-mentioned equation naturally constitutes a recursive scheme due to

$$G_k^-(t + \Delta t) = \theta_k G_k^-(t) + \int_0^{\Delta t} \beta_k e^{p_k \tau} A^-(t + \Delta t - \tau) d\tau; \quad \theta_k = e^{p_k \Delta t}. \quad (12)$$

Numerically, a second-order trapezoidal quadrature rule<sup>18</sup> is applied to evaluate Eq. (12). The incident wave  $A^-(t + \Delta t)$  is given by the first-order extrapolation at  $y = 0$  suggested by Scalo *et al.*,<sup>23</sup>

$$A^-(y, t + \Delta t) = v'(y, t + \Delta t) - p'_a(y, t + \Delta t) \\ \approx v'(y + a_w \Delta t, t) - p'_a(y + a_w \Delta t, t), \quad (13)$$

which eventually gives rise to an iterative scheme of  $A^-$ ,

$$A^-(y, t + \Delta t) \approx \underbrace{v'(y, t) - p'_a(y, t)}_{A^-(y, t)} + a_w \Delta t \frac{\partial \{v'(y, t) - p'_a(y, t)\}}{\partial y}. \quad (14)$$

Given the incident wave amplitude  $A^-(t + \Delta t)$ , the reflection wave  $A^+(t + \Delta t)$  is obtained by Eq. (10). Subsequently, the wall-normal velocity at the next time step is updated by

$$v'(t + \Delta t) = (A^+ + A^-)/2 = \text{Re} \left( \sum_{k=1}^{n_k} G_k^-(t + \Delta t) \right), \quad (15)$$

while  $p'$  is calculated via Eq. (7),

$$p'(t + \Delta t) = \{A^+(t + \Delta t) - A^-(t + \Delta t)\} \bar{\rho}_w \bar{a}_w / 2. \quad (16)$$

Finally, the instantaneous wall-normal velocity and pressure on the wall boundary are obtained by superimposition on the corresponding base-flow variables.

### C. Modified time-domain impedance boundary condition (MTDIBC)

As aforementioned in Sec. I, we are interested in revealing to what degree the fluctuations  $p'$  and  $v'$  can be decoupled and how  $p'$  and  $v'$  interplay. In fact, the difference between a smooth wall and a porous wall (acoustic metasurface) appears to be that mass and momentum transfer occurs across the micro-cavities. We hereupon raise two questions: (1) Can we approximate the acoustic metasurface as an unsteady wall blowing-suction strip? (2) What is the role of unsteadiness in stabilizing the broadband disturbance? For the latter question, if unsteadiness is unimportant, the extreme state is that a steady blowing suction behaves similarly to the original unsteady blowing suction. If this state is not the fact, a critical timescale or frequency may be found.

To answer the above-mentioned questions, we modify the conventional TDIBC model to perform numerical experiments. First, DNS with the conventional TDIBC is performed first. During the simulation, the wall-normal velocity dataset at  $y = 0$  in the metasurface region is output at every time steps and stored on the hard disk. Using this dataset of  $v'$  as an unsteady wall boundary condition at each mesh point, we perform another DNS. The updating procedure of wall pressure, i.e., Eq. (16), is replaced by  $\partial p / \partial y = 0$ , which is commonly employed in N-S solvers. This Neumann condition gives the wall pressure based on the known pressure of the nearest node in the wall-normal direction, i.e., a simple first-order approximation. This



enforced condition, called modified TDIBC or “MTDIBC,” allows the pressure on the wall boundary to be updated passively by the wall-normal velocity fluctuation  $v'$ . Therefore, this MTDIBC resembles a response problem to an unsteady wall blowing-suction strip.

To further assess the significance of unsteadiness, the stored time series at each mesh point are temporally filtered by a tenth-order Butterworth low-pass filter with a cutoff frequency  $f_c^*$ . The filtered time series is shifted to minimize the time delay by checking the cross correlation function. The high-frequency components above  $f_c^*$  are removed, while those below  $f_c^*$  are maintained. As  $f_c^*$  is decreased, wider band of frequency components are removed by the filter, and the model becomes away from the original blowing-suction model without filtering. Totally, a MTDIBC case without filtering and six MTDIBC cases with different cutoff frequencies are simulated, including  $f_c^* = 400, 350, 300, 250, 200$ , and  $150$  kHz. For example, if the DNS case with  $f_c^* = 400$  kHz successfully reproduces the result of the one without filtering, the frequency band above 400 kHz is regarded as unimportant.

#### D. Multi-pole approximation of wall softness

The determination of the conjugate pairs of poles and residues in Eq. (9) is not unique. Algorithms, such as the iterative least squares fitting in Ref. 20, enable a satisfactory fitting to the discrete dataset provided by either experimental results or reliable impedance models. When the frequency exceeds 300 kHz in the considered broadband disturbance, these spectral components decay rapidly for both metasurface and TDIBC cases (shown later). Thus, we only concentrate on the fitting of the acoustic wall softness below 300 kHz. Figure 3 shows an excellent fitting agreement within the frequency range of interest. Meanwhile, in the considered flat-plate boundary layer, Fig. 3 illustrates that the wall softness  $W(\omega)$  calculated based on the impedance model<sup>37</sup> is entirely insensitive to the selection of the streamwise location for base-flow quantities. Ten conjugate pairs of poles and residues are applied in the final fitting function, where the information is detailed in Table I.

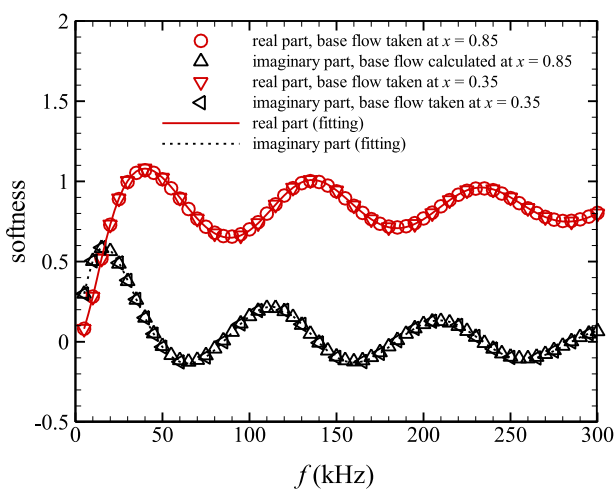


FIG. 3. Comparison of wall softness  $W(\omega)$  between the impedance model<sup>37</sup> (symbols) and the multi-pole fitting results (lines).

TABLE I. Conjugate pairs of dimensionless poles and residues.

Pair number ( $k$ )	Poles ( $p_k$ )	Residues ( $\beta_k$ )
1	(−111.980, 595.313)	(109.678, 20.631)
2	(−203.277, 3871.378)	(269.167, 14.133)
3	(−48.977, −209.187)	(32.931, −7.710)
4	(−10.673, −0.033)	(0.798, −259.963)
5	(−17.116, −997.046)	(146.984, −2.523)
6	(−1145.867, 297.759)	(58.582, 225.439)
7	(−325.950, −2670.483)	(204.960, −25.017)
8	(−329.014, 2729.641)	(248.601, 29.965)
9	(−88.475, −360.592)	(55.609, −13.644)
10	(−52.805, 28.276)	(55.756, 104.123)

### III. RESULTS

#### A. Prediction discrepancy between TDIBC and metasurface cases

Before focusing on the physics, the origin of the prediction discrepancy between the TDIBC and the metasurface should be analyzed first. This analysis is expected to reflect the comprehensive effect of the metasurface with microstructures (rather than the impedance boundary condition) on the broadband wave packet, which is hardly documented in the literature.

##### 1. Single-frequency-disturbance case

Starting from a steady solution at  $t = 0$ , the propagating single-frequency instability wave finally penetrates the metasurface region  $0.2 < x < 1$ . Figure 4 shows that the TDIBC model is entirely consistent with the direct coupling method for a constant wall impedance. Compared to the metasurface case, these models slightly underestimate the pressure fluctuation. It is also observed that the maximum pressure fluctuation of the impedance models approaches the lower

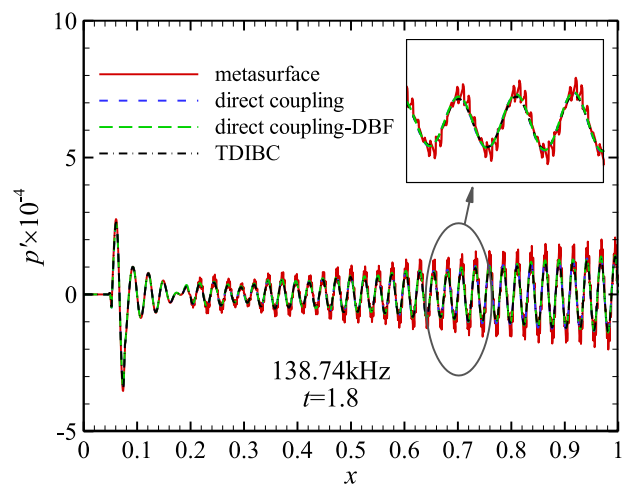


FIG. 4. Comparison of the pressure fluctuation along  $y = 0$  for the single-frequency case at  $t = 1.8$ .

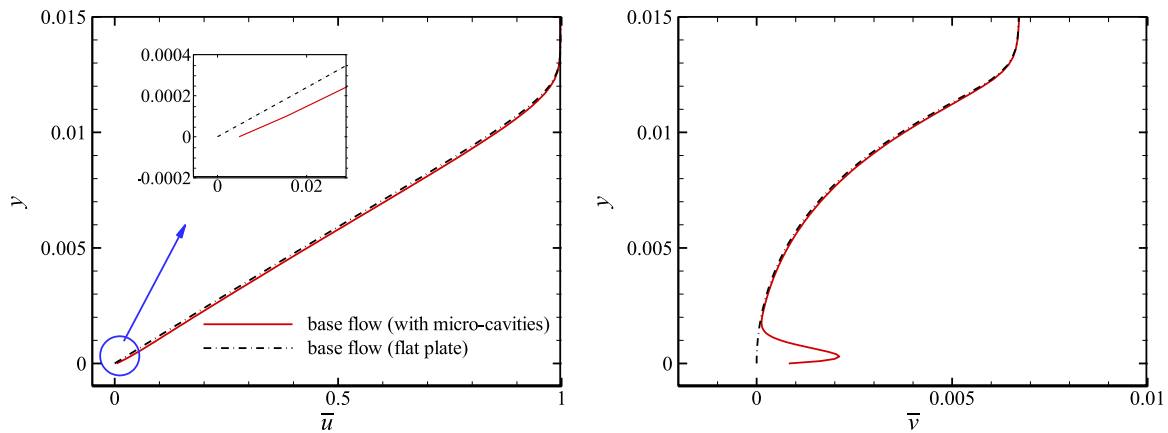


FIG. 5. The cavity-induced distortion in the base flow streamwise velocity (left) and wall-normal velocity (right) at  $x = 0.8$ , which is at the three-quarter length of the cavity.

bound of the streamwise oscillating fluctuation of the metasurface case. This is consistent with the observation in Ref. 17 under the same condition (Fig. 7 in Ref. 17). The streamwise oscillation of  $p'$  in the metasurface case has also been reported in Ref. 17.

It is preliminarily deduced from Fig. 4 that the minor deviation between the impedance models and the metasurface does not result from the numerical error by the TDIBC procedures, such as the extrapolation or convolution manipulation, since the direct coupling method does not involve these effects. In addition, as shown in Fig. 5, the micro-cavities of the metasurface can distort the near-wall base flow profiles via mass transfer across the shear layer. To consider this effect, the 2D base flow of the direct-coupling-method case, i.e., the flat-plate boundary layer, is replaced with that of the metasurface corresponding to the solid lines in Fig. 5. The wall boundary condition is

adjusted to allow the velocity slip and penetration as is in the metasurface case. The corresponding result is given in Fig. 4 labeled as “direct coupling-DBF” (i.e., distorted base flow), which nearly overlaps with the counterpart of the original direct coupling method. Therefore, the deviation between the TDIBC and the metasurface is not attributed to the base-flow-distortion effect induced by micro-cavities. The responsible effect is, thus, inferred to be the minor impedance modeling error.

## 2. Broadband-disturbance case

Figure 6 further displays the 2D pressure and wall-normal velocity fluctuations between the metasurface (contour) and TDIBC (dashed line) cases at two instants. The near-field wave packet as well

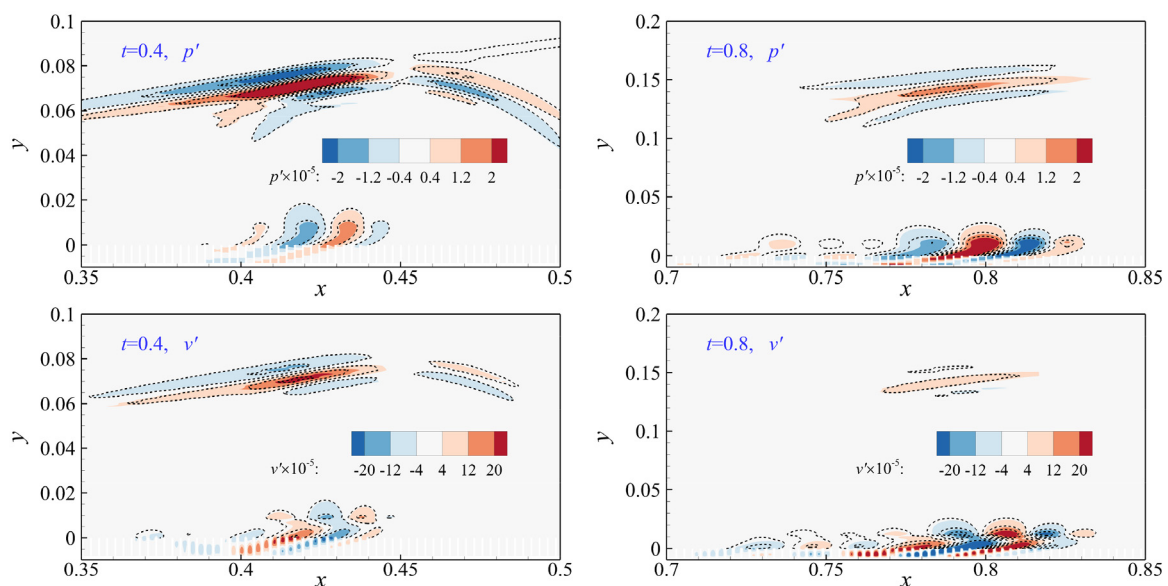


FIG. 6. Contours of the pressure and wall-normal velocity fluctuations at  $t = 0.4$  (left) and  $t = 0.8$  (right) for the metasurface (contour) and TDIBC (dashed line) broadband-disturbance cases.

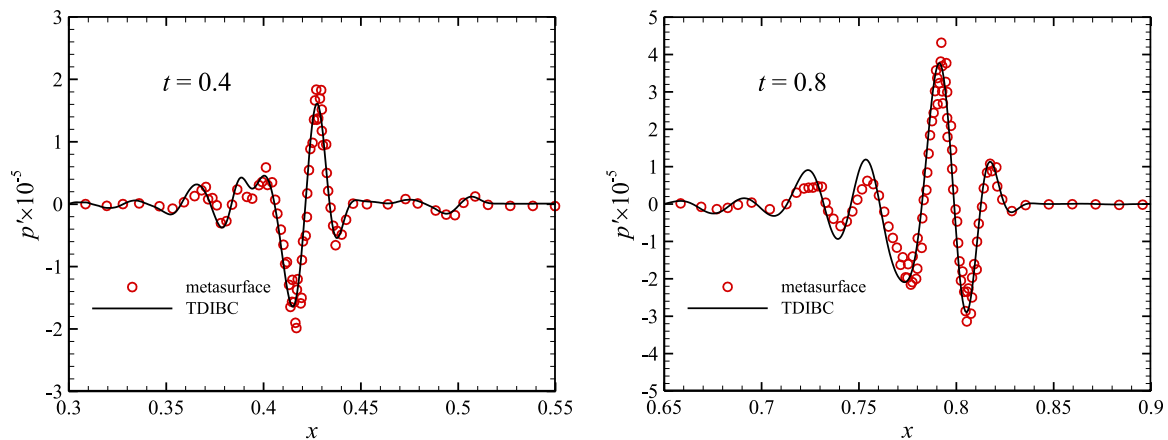


FIG. 7. Comparison of the pressure fluctuation for the broadband-disturbance case at  $t = 0.4$  (left) and  $t = 0.8$  (right) along  $y = 0$  between the metasurface and TDIBC.

as the far-field propagating wave interacting with the leading-edge oblique shock wave is well captured. The peak and valley characteristics are accurately given by TDIBC, particularly for the downstream wave front region. Quantitatively, Fig. 7 compares the instantaneous pressure fluctuation along  $y = 0$  at  $t = 0.4$  and  $0.8$ . The amplitude and phase information is satisfactorily predicted by TDIBC. The main discrepancy is observed in the tail region of the wave packet. This discrepancy is inferred to be caused by the first-mode band, since it has a lower phase speed than the second-mode instability. Other potential effects, such as dissipation induced by the micro-cavity flow, may also be responsible for this discrepancy. Generally, it is found that the overall effect of the metasurface with microstructures can be well modeled by TDIBC. The depicted agreement enables several further DNS studies without meshing the cavity flows and examining the aforementioned wall blowing-suction approximation.

## B. Physical effect of metasurface on broadband wave packet

### 1. Wall blowing-suction approximation

In this section, the DNS results given by MTDIBC without filtering and with different cutoff frequencies of the filter are discussed. Figure 8 shows the effect of the low-pass filter on the time series of  $v'$ . As  $f_c^*$  is decreased, the time series gradually deviates from the one without filtering. This deviation appears not to be significant when  $f_c^*$  exceeds around 300 kHz. Figure 9 compares the maximum pressure fluctuation in history between the metasurface, the TDIBC, and the MTDIBC cases for broadband disturbances. Result of a smooth-wall boundary layer case without any metasurface or impedance boundary is also shown. The metasurface region starting from  $x = 0.2$  effectively suppresses the peak pressure fluctuation. Although streamwise oscillation occurs in the metasurface case (also reported in Ref. 17), the curve of the TDIBC case falls within the scattered one of the metasurface case. Using the  $v'$  dataset of the TDIBC case on the wall as an unsteady input for the wall boundary condition, the MTDIBC case without

temporal filtering successfully reproduces the result of the conventional TDIBC with minor bias. Similar reproduction by the MTDIBC case without filtering is observed in Fig. 10, which shows the wall distribution of  $p'$  at  $t = 0.4$ . The resemblance indicates that the metasurface can be approximated by an unsteady wall blowing-suction model. This model works in the following procedure: (1) the wave packet propagates past the metasurface region, (2) mass transfer occurs across the micro-cavities, (3) wall-normal velocity fluctuation  $v'$  increases, and (4) passive response of  $p'$  occurs accordingly where a Neumann boundary condition  $\partial p / \partial y = 0$  is imposed. Hereupon, it is of particular interest to examine how the unsteadiness of the wall blowing-suction model determines the response of  $p'$ . This study may further the understanding of the stabilization effect of the metasurface on the wave packet, particularly on those second-mode components of acoustic nature.

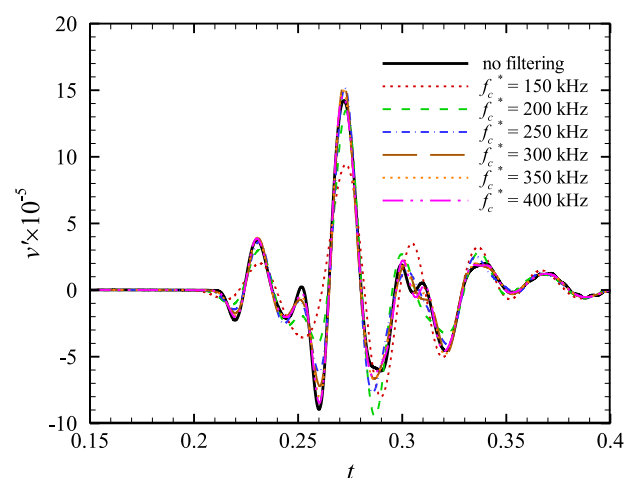
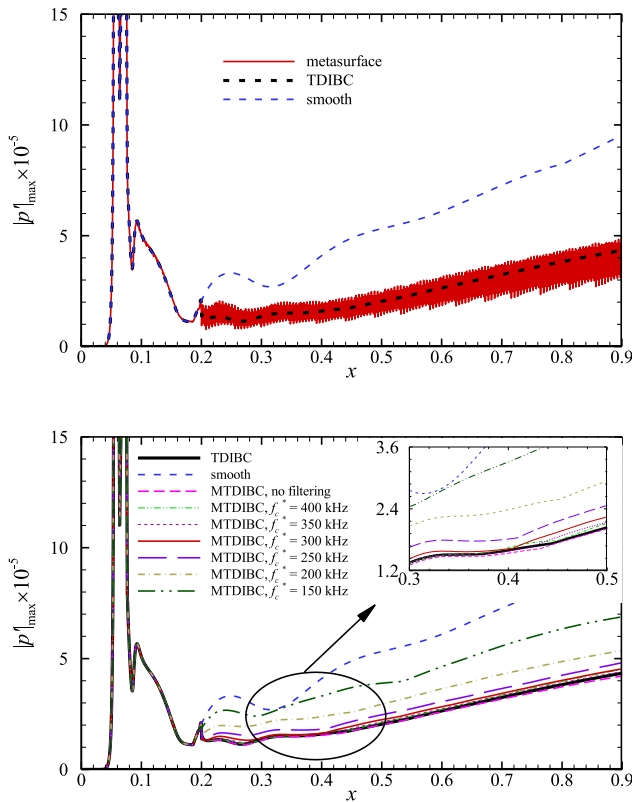


FIG. 8. Time history of the wall-normal velocity fluctuation at  $(x, y) = (0.3, 0)$  for MTDIBC cases without filtering and with different cutoff frequencies  $f_c^*$ .





**FIG. 9.** Comparison of the maximum pressure fluctuation along  $y=0$  for the TDIBC and metasurface cases (top) and for MTDIBC with different cutoff frequencies  $f_c^*$  (bottom).

As  $f_c^*$  is decreased, wider high-frequency bands are removed in the DNS with MTDIBC. It is observed that the case  $f_c^* = 300$  kHz starts to fail to reproduce the stabilization effect of the impedance boundary in Fig. 9 and the shape of the wave packet in Fig. 10. The

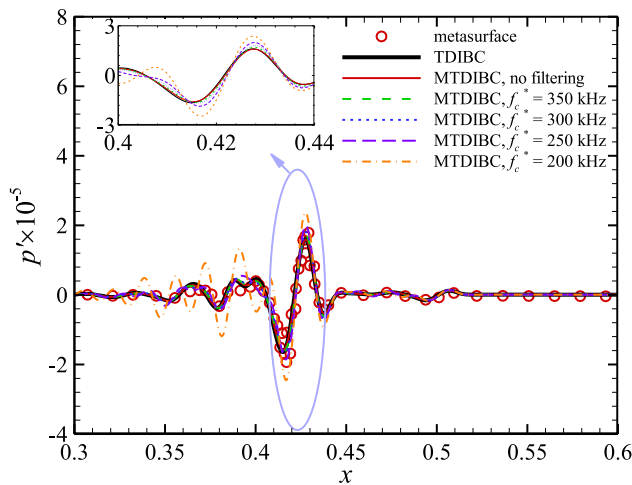


**FIG. 10.** Comparison of the pressure fluctuation at  $t=0.4$  along  $y=0$  between the cases with the metasurface, TDIBC, and MTDIBC with different cutoff frequencies  $f_c^*$ .

case  $f_c^* = 200$  kHz performs even worse, and the case  $f_c^* = 150$  kHz nearly approaches the smooth-wall case in Fig. 9. Accordingly, the case  $f_c^* = 300$  kHz can be roughly regarded as a critical point, above which the difference between TDIBC and MTDIBC cases is non-negligible. Figure 11 further shows the contours of  $p'$  and  $v'$  at  $t=0.4$  for TDIBC and MTDIBC cases (top) and the smooth-wall case (bottom). The  $p'$  contour of the wave packet by the MTDIBC case without filtering (solid line) agrees well with that by the TDIBC case, whereas the MTDIBC case with  $f_c^* = 200$  kHz (dashed line) deviates from the baseline TDIBC case. These observations confirm the success of the unsteady wall blowing-suction model and the significance of the low-frequency components below a critical frequency. In addition, comparison between the TDIBC and smooth-wall cases shows that the near-wall region roughly in  $y < 0.002$  reports the main suppression of pressure fluctuations. The mechanism behind will be discussed by an energy analysis later.

To locate the critical frequency in the broadband spectrum, two selected probes at  $x=0.3$  and at  $x=0.5$  are chosen to present the wall pressure and wall-normal velocity spectra, as shown in Fig. 12. The pressure frequency band of around (100 and 300 kHz) is considerably stabilized by the impedance wall boundary, while lower-frequency band is marginally destabilized. The most unstable frequency is also reduced by the impedance boundary condition. These observations are consistent with previous experimental findings by Fedorov *et al.*<sup>14</sup> To further check the filter effect, the wall-normal velocity spectra are examined in Fig. 12. Only a small proportion of energetic components are distributed above the critical frequency  $f_c^* = 300$  kHz. However, Figs. 9–11 have shown that the pressure response is sensitive to the absence of these high-frequency components above the critical value. It is, thus, concluded that the high-frequency unsteadiness of the wall blowing-suction behavior is indispensable to reproduce the stabilization effects on the wave packet by the metasurface, although the carried energy (Fig. 12) and distortion of  $v'$  (Fig. 8) by these high-frequency components are not major.

## 2. Energy analysis

Energy analysis is further employed to reveal the physical mechanism of the overall stabilization effect of the metasurface. Although similar approach has been applied in the single-frequency scenario,<sup>33</sup> the effect on the broadband wave packet has hardly been discussed. Note that the base flow above the cavity, i.e.,  $y > 0$ , is not significantly affected compared to the smooth-wall boundary layer and that the TDIBC is observed to predict the propagation of the broadband disturbance accurately. Consequently, the TDIBC case is used for the energy analysis. For a comprehensive consideration, Chu's energy norm<sup>38</sup> is used, which consists of the kinetic energy and a strictly positive definite fluctuating thermodynamic energy. The detailed definition of Chu's energy density is given by

$$E_{\text{Chu}}(x, y) = \frac{1}{2} \left[ \bar{\rho} (u'^2 + v'^2) + \frac{\bar{p}}{\bar{\rho}^2} \rho'^2 + \frac{\bar{p}}{(\gamma - 1) \bar{T}^2} T'^2 \right]. \quad (17)$$

Following the derivation of Hao and Wen,<sup>33</sup> the budget equation of the time-averaged Chu's energy for small-amplitude disturbance is written as follows:

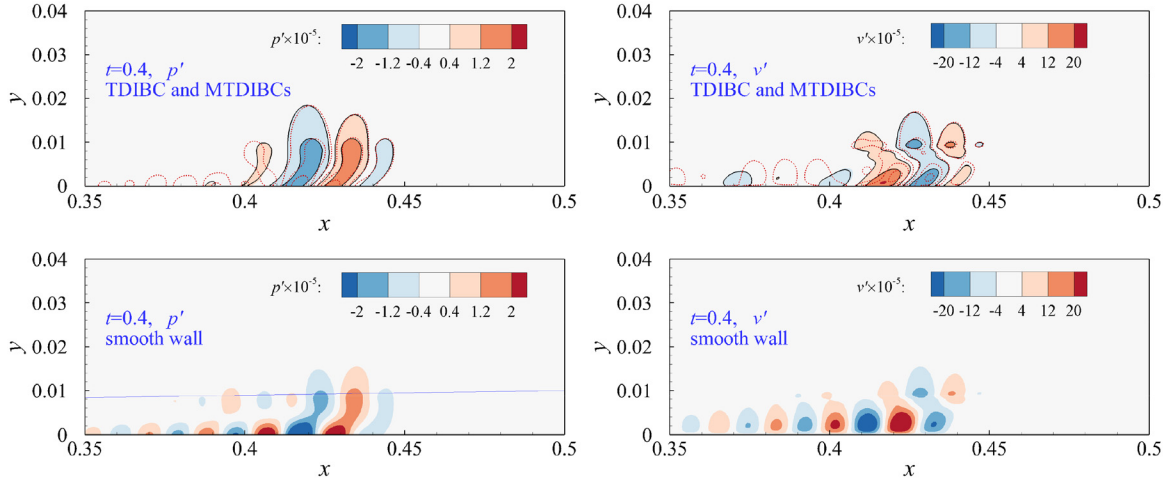


**FIG. 11.** Contours of the pressure and wall-normal velocity fluctuations at  $t = 0.4$  for the TDIBC (top) and smooth-wall (bottom) cases. Lines in the top panel: MTDIBC without filtering (solid line) and with  $f_c^* = 200$  kHz (dashed line). Thin line in the bottom panel: location of the boundary layer nominal thickness.

$$\begin{aligned}
 \bar{u}_j \frac{\partial \bar{E}_{\text{Chu}}}{\partial x_j} = & \underbrace{-\overline{u'_i(\rho u_j)'}}_{\text{Reynolds stress work}} - \underbrace{\frac{\bar{p}}{\rho^2} \overline{\rho' u'_j} \frac{\partial \bar{\rho}}{\partial x_j} - \frac{\bar{p}}{(\gamma-1)T^2} \overline{T' u'_j} \frac{\partial \bar{T}}{\partial x_j}}_{\text{Thermal stress work}} \\
 & \underbrace{-\overline{u'_i \frac{\partial \bar{p}'}{\partial x_i}} - \frac{\bar{p}}{\rho^2} \overline{\rho' \left( \rho \frac{\partial u_j}{\partial x_j} \right)'}}_{\text{Dilatation related work}} - \underbrace{\frac{\bar{p}}{T^2} \overline{T' \left( T \frac{\partial u_j}{\partial x_j} \right)'}}_{\text{Viscous related work}} \\
 & + \underbrace{\frac{1}{Re_\infty} \left\{ \overline{u'_i \frac{\partial \sigma'_{ij}}{\partial x_j}} + \frac{1}{T} \overline{T' \left( \sigma_{ij} \frac{\partial u_i}{\partial x_j} \right)'} - \frac{1}{T} \overline{T' \frac{\partial q'_j}{\partial x_j}} \right\}}_{\text{Nonparallel-effect work}} \\
 & + \frac{1}{2} \left\{ \overline{\rho' \bar{u}_j} \frac{\partial}{\partial x_j} \left( \frac{\bar{p}}{\rho^2} \right) + \overline{u'_i \bar{u}_j} \frac{\partial \bar{\rho}}{\partial x_j} + \overline{T' T' \bar{u}_j} \frac{\partial}{\partial x_j} \left( \frac{\bar{p}}{T^2} \right) \right\},
 \end{aligned} \quad (18)$$

where  $i$  and  $j$  are Einstein notation indexes. The left-hand side denotes the net energy variation arising from the right-hand-side source or sink. The first right-hand-side work in the bracket is done by the Reynolds stress fluctuation on the mean flow gradient. The second one is done by the thermal stress fluctuation on the mean density and temperature gradients. The third one is done by the dilatation-related fluctuation induced by compressibility. The fourth one is done by the viscous diffusion and dissipation fluctuations associated with molecular transport. The last one is done arising from the non-parallel-flow effect, which is found to be ignorable and, thus, omitted in the present paper.

Figure 13 displays the contours of possible source terms for energy growth, including the Reynolds stress work, thermal stress work, and dilatation related work. The thermal stress work is dominant in the region approaching the boundary layer edge, which is related to the inviscid instability mechanism near the critical layer. However, the thermal work is not considerably changed by the metasurface. In contrast, the dilatation related work is evidently suppressed

by the metasurface just downstream of the starting position at  $x = 0.2$ . The suppressed region falls within the wall-normal range  $y < 0.002$  in Fig. 11, where the wave packet gets attenuated. Since the near-wall growth of the fluctuation is of primary interest, the concerned terms are further plotted in Fig. 14 at  $x = 0.25$ . The role of the viscous related work can be regarded as passively balancing the source terms, which contributes to a small net energy change. Nevertheless, the notably decreased dilatation eventually results in the sign of net energy change varying from positive (smooth wall) to negative (TDIBC). Therefore, the suppressed dilatation related work accounts for the initial attenuation of the pressure fluctuation by the metasurface in the vicinity of  $x = 0.25$  in Fig. 9. This finding also shares a similarity with Kuehl's thermoacoustic explanation<sup>34</sup> that the dilatation-related divergence of acoustic power  $\nabla \cdot (pV)'$  is dominant in the near-wall region for the second-mode instability. Furthermore, the dilatation-dominated conclusion differs from that by our previous investigation<sup>33</sup> on flows past a large-scale shallow cavity. In that study, the mean velocity gradient  $\partial \bar{u} / \partial y$  was reduced near the shear layer of the cavity flow, which rendered the Reynolds shear stress work to be responsible for the suppression of the second mode. By contrast, the present metasurface possesses micro-cavities with a longitudinal width smaller than the second-mode wavelength. It can be understood from Fig. 5 that the mean streamwise velocity gradient  $\partial \bar{u} / \partial y$  is nearly unaffected by the micro-cavity flow and that the change in Reynolds stress work does not account for the stabilization effect of the metasurface.

#### IV. CONCLUSION

TDIBC is coupled with an N-S solver to perform direct numerical simulations on a Mach 6 boundary layer. Through a careful comparative study with an acoustic metasurface with micro-cavities, the conventional TDIBC model is shown to predict the propagation of both single-frequency and broadband disturbances accurately. Based on the case studies, the minor discrepancy in the wall fluctuation is found to arise from the impedance modeling error rather than the effects of numerical aspects or cavity-induced base flow distortion. For a broadband pulse, the discrepancy between TDIBC and the

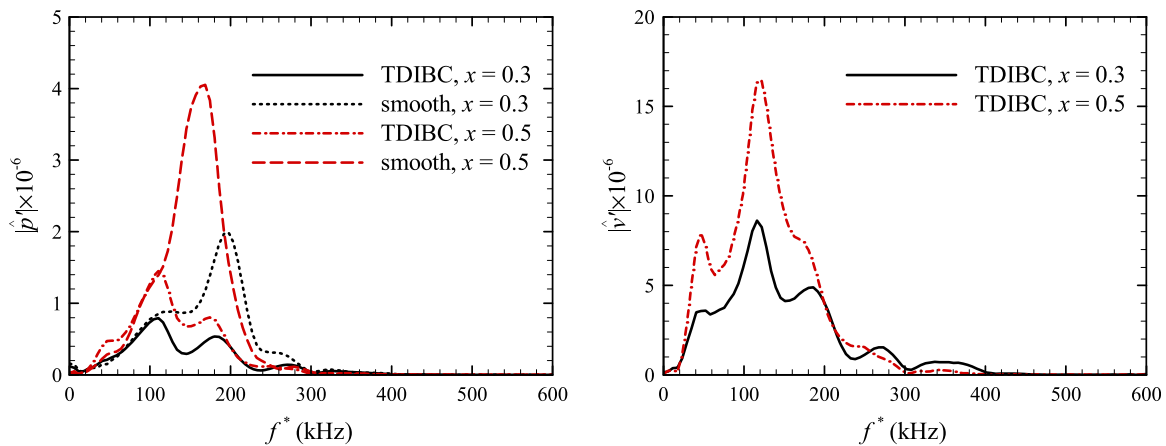


FIG. 12. Wall pressure spectra for TDIBC and smooth-wall cases (left) and wall-normal velocity spectra for TDIBC cases (right) at  $x = 0.3$  and  $0.5$ .

metasurface is mainly observed in the tail of the wave packet. Numerical experiments demonstrate that the metasurface can be approximated as an equivalent unsteady blowing-suction model to perturb the wall-normal velocity and then passively the pressure. The pressure can be decoupled to be updated by the Neumann condition, as usually employed in Navier–Stokes solvers. The dominant frequency scale that enables reproducing the stabilization effect of the metasurface is found to be slightly smaller than the energetic frequency maximum of the wave packet. This finding indicates that the high-frequency unsteadiness nature of the blowing-suction behavior is indispensable. Physically, the stabilization mechanism of the acoustic

metasurface from an energy consideration is that the near-wall dilatation-related work due to compressibility is significantly damped by the metasurface. Owing to this largely decreased source term, the sign of the near-wall net change in Chu’s energy is altered from positive to negative. This decreased region also agrees with the wall-normal location, where the wave packet fluctuations are suppressed by the metasurface. Thus, the initial reduction in the maximum wall pressure fluctuation in the early metasurface region can be understood.

The present work points out to what degree the TDIBC can be applied in the study and design of the metasurface. The work sheds

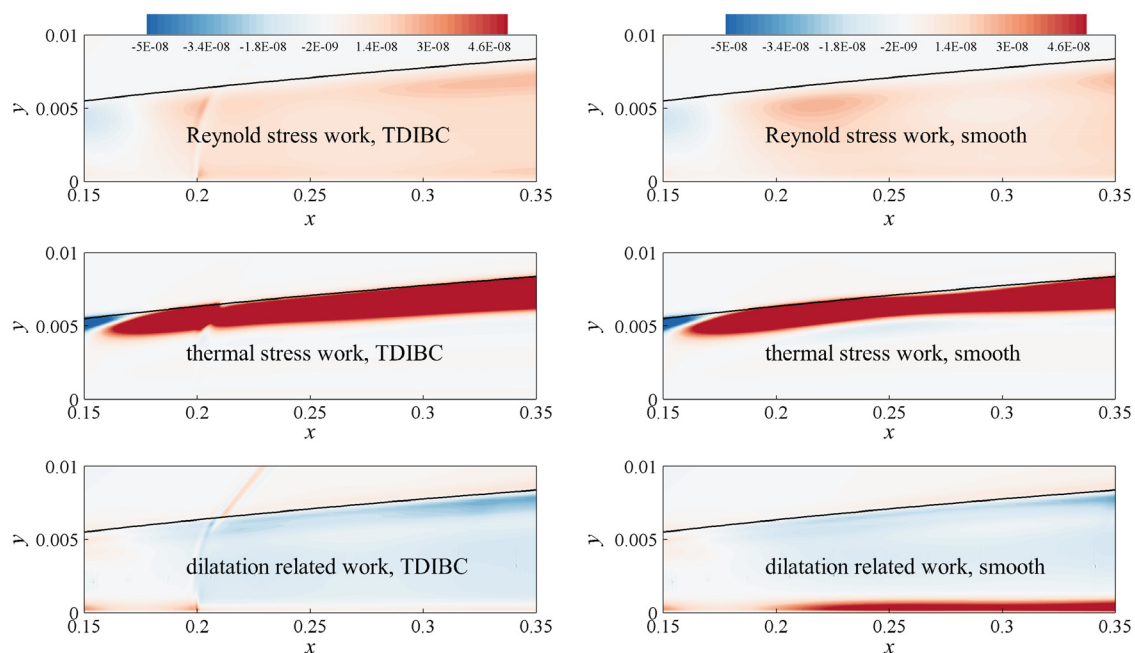


FIG. 13. Contours of the energy source terms in Eq. (18) for TDIBC and smooth wall cases. Solid line: location of the boundary layer thickness. Starting location of TDIBC:  $x = 0.2$ .

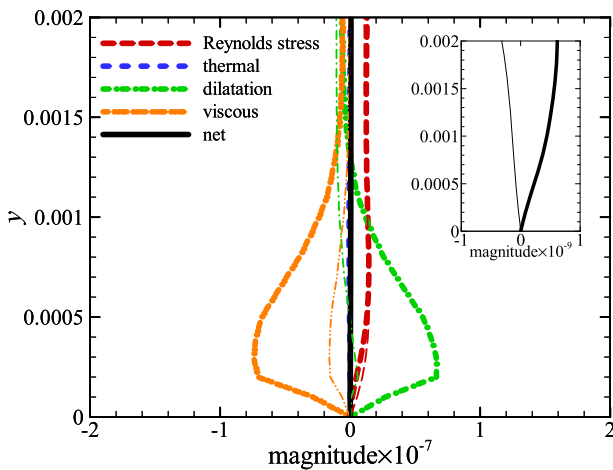


FIG. 14. Distribution of energy source terms in Eq. (18) in the near-wall region for smooth (thick line) and TDIBC wall (thin line) cases at  $x = 0.25$ .

light on the physical role of the metasurface in controlling broadband disturbances based on both model approximation and energy analysis.

## ACKNOWLEDGMENTS

This research was supported by the Research Grants Council, Hong Kong (Grant Nos. 15216621 and 15206519) and the National Natural Science Foundation of China (Grant No. 12272049). We express our honest appreciation to Professor Xinliang Li for his generosity in providing the DNS code.

## AUTHOR DECLARATIONS

### Conflict of Interest

The authors have no conflicts to disclose.

## Author Contributions

**Peixu Guo:** Conceptualization (lead); Formal analysis (lead); Investigation (lead); Methodology (lead); Validation (equal); Writing – original draft (lead); Writing – review & editing (lead). **Xiao Liu:** Investigation (supporting); Software (equal); Validation (equal); Writing – original draft (supporting). **Rui Zhao:** Formal analysis (supporting); Funding acquisition (equal); Software (equal); Writing – original draft (supporting). **Jiaao Hao:** Formal analysis (supporting); Resources (equal); Writing – original draft (supporting). **Chih-Yung Wen:** Formal analysis (supporting); Funding acquisition (equal); Resources (equal); Writing – original draft (supporting).

## DATA AVAILABILITY

The data that support the findings of this study are available from the corresponding author upon reasonable request.

## REFERENCES

- <sup>1</sup>H. Men, X. Li, and H. Liu, “Direct numerical simulations of hypersonic boundary layer transition over a hypersonic transition research vehicle model lifting body at different angles of attack,” *Phys. Fluids* **35**, 044111 (2023).

- <sup>2</sup>H. Ren, S. Wang, X. Yuan, J. Chen, Y. Zhang, and X. Xiang, “A flight test based deep learning method for transition heat flux prediction in hypersonic flow,” *Phys. Fluids* **34**, 054106 (2022).
- <sup>3</sup>L. M. Mack, “Linear stability theory and the problem of supersonic boundary-layer transition,” *AIAA J.* **13**, 278–289 (1975).
- <sup>4</sup>I. Leyva, J. Jewell, S. Laurence, H. Hornung, and J. Shepherd, “On the impact of injection schemes on transition in hypersonic boundary layers,” AIAA Paper No. 2009-7204, 2009.
- <sup>5</sup>A. V. Fedorov, V. Soudakov, and I. A. Leyva, “Stability analysis of high-speed boundary-layer flow with gas injection,” AIAA Paper No. 2014-2498, 2014.
- <sup>6</sup>A. V. Fedorov, V. Soudakov, and I. A. Leyva, “Stabilization of hypersonic boundary layers by porous coatings,” *AIAA J.* **39**, 605–610 (2001).
- <sup>7</sup>W. Zhu, D. Gu, W. Si, S. Chen, Y. Zhu, and C. Lee, “Reduced aerodynamic heating in a hypersonic boundary layer by a wavy wall,” *Sci. Bull.* **67**, 988–990 (2022).
- <sup>8</sup>W. Zhu, D. Gu, W. Si, M. Zhang, S. Chen, C. Smith, Y. Zhu, and C. Lee, “Instability evolution in the hypersonic boundary layer over a wavy wall,” *J. Fluid Mech.* **943**, A16 (2022).
- <sup>9</sup>R. Zhao, C. Wen, Y. Zhou, G. Tu, and J. Lei, “Review of acoustic metasurfaces for hypersonic boundary layer stabilization,” *Prog. Aerosp. Sci.* **130**, 100808 (2022).
- <sup>10</sup>X. Tian, T. Liu, T. Wang, J. Zhu, and C. Wen, “Double-layer acoustic metasurface for the suppression of the Mack second mode in hypersonic boundary-layer flow,” *Phys. Fluids* **34**, 074105 (2022).
- <sup>11</sup>V. C. B. Sousa, V. Wartemann, A. Wagner, and C. Scalzo, “Linear stability analysis of second-mode attenuation via porous carbon-matrix ceramics,” *Phys. Fluids* **35**, 064113 (2023).
- <sup>12</sup>N. Malmuth, A. Fedorov, V. Shalae, J. Cole, D. Williams, M. Hites, and A. Khokhlov, “Problems in high speed flow prediction relevant to control,” AIAA Paper No. 1998-2695, 1998.
- <sup>13</sup>A. Rasheed, H. G. Hornung, A. V. Fedorov, and N. D. Malmuth, “Experiments on passive hypervelocity boundary-layer control using an ultrasonically absorptive surface,” *AIAA J.* **40**, 481–489 (2002).
- <sup>14</sup>A. Fedorov, A. Shiplyuk, A. Maslov, E. Burov, and N. Malmuth, “Stabilization of a hypersonic boundary layer using an ultrasonically absorptive coating,” *J. Fluid Mech.* **479**, 99–124 (2003).
- <sup>15</sup>P. W. Carpenter and L. J. Porter, “Effects of passive porous walls on boundary-layer instability,” *AIAA J.* **39**, 597–604 (2001).
- <sup>16</sup>X. Tian, R. Zhao, T. Long, and C. Y. Wen, “Reverse design of ultrasonic absorptive coating for the stabilization of Mack modes,” *AIAA J.* **57**, 2264–2269 (2019).
- <sup>17</sup>R. Zhao, C. Y. Wen, T. H. Long, X. D. Tian, L. Zhou, and Y. Wu, “Spatial direct numerical simulation of the hypersonic boundary-layer stabilization using porous coatings,” *AIAA J.* **57**, 5061–5065 (2019).
- <sup>18</sup>K. Y. Fung and H. Ju, “Time-domain impedance boundary conditions for computational acoustics and aeroacoustics,” *Int. J. Comput. Fluid Dyn.* **18**, 503–511 (2004).
- <sup>19</sup>S. Jaensch, C. Sovardi, and W. Polifke, “On the robust, flexible and consistent implementation of time domain impedance boundary conditions for compressible flow simulations,” *J. Comput. Phys.* **314**, 145–159 (2016).
- <sup>20</sup>Q. Douasbin, C. Scalzo, L. Selle, and T. Poinot, “Delayed-time domain impedance boundary conditions (D-TDIBC),” *J. Comput. Phys.* **371**, 50–66 (2018).
- <sup>21</sup>F. Monteghetti, D. Matignon, and E. Piot, “Energy analysis and discretization of nonlinear impedance boundary conditions for the time-domain linearized Euler equations,” *J. Comput. Phys.* **375**, 393–426 (2018).
- <sup>22</sup>R. Fiévet, H. Deniau, and E. Piot, “Strong compact formalism for characteristic boundary conditions with discontinuous spectral methods,” *J. Comput. Phys.* **408**, 109276 (2020).
- <sup>23</sup>C. Scalzo, J. Bodart, and S. K. Lele, “Compressible turbulent channel flow with impedance boundary conditions,” *Phys. Fluids* **27**, 035107 (2015).
- <sup>24</sup>Y. Chen and C. Scalzo, “Trapped waves in supersonic and hypersonic turbulent channel flow over porous walls,” *J. Fluid Mech.* **920**, A24 (2021).
- <sup>25</sup>J. Lin, C. Scalzo, and L. Hesselink, “High-fidelity simulation of a standing-wave thermoacoustic-piezoelectric engine,” *J. Fluid Mech.* **808**, 19–60 (2016).
- <sup>26</sup>V. C. Sousa, D. Patel, J. B. Chapelier, V. Wartemann, A. Wagner, and C. Scalzo, “Numerical investigation of second-mode attenuation over carbon/carbon porous surfaces,” *J. Spacecr. Rockets* **56**, 319–332 (2019).

- <sup>27</sup>R. Fiévet, H. Deniau, J. P. Brazier, and E. Piot, "Numerical analysis of porous coatings stabilizing capabilities on hypersonic boundary-layer transition," *AIAA J.* **59**, 3845–3858 (2021).
- <sup>28</sup>J. Sivasubramanian and H. F. Fasel, "Numerical investigation of the development of three-dimensional wavepackets in a sharp cone boundary layer at Mach 6," *J. Fluid Mech.* **756**, 600–649 (2014).
- <sup>29</sup>P. Guo, F. Shi, Z. Gao, C. Jiang, C. H. Lee, and C. Y. Wen, "Sensitivity analysis on supersonic-boundary-layer stability: Parametric influence, optimization, and inverse design," *Phys. Fluids* **34**, 104113 (2022).
- <sup>30</sup>P. Guo, Z. Gao, C. Jiang, and C. H. Lee, "Sensitivity analysis on supersonic-boundary-layer stability subject to perturbation of flow parameters," *Phys. Fluids* **33**, 084111 (2021).
- <sup>31</sup>P. Guo, F. Shi, Z. Gao, C. Jiang, C. H. Lee, and C. Y. Wen, "Heat transfer and behavior of the Reynolds stress in Mach 6 boundary layer transition induced by first-mode oblique waves," *Phys. Fluids* **34**, 104116 (2022).
- <sup>32</sup>Y. Chen, P. Guo, and C. Y. Wen, "A unified explanation of energy growth sources for unstable modes in flat-plate boundary layers," *J. Fluid Mech.* (in press) (2023).
- <sup>33</sup>J. Hao and C. Y. Wen, "Stabilization of a two-dimensional hypersonic boundary layer using a shallow cavity," *AIAA J.* **59**, 430–438 (2021).
- <sup>34</sup>J. J. Kuehl, "Thermoacoustic interpretation of second-mode instability," *AIAA J.* **56**, 3585–3592 (2018).
- <sup>35</sup>D. Bountin, T. Cchimitov, and A. Maslov, "Stabilization of a hypersonic boundary layer using a wavy surface," *AIAA J.* **51**, 1203–1210 (2013).
- <sup>36</sup>R. Zhao, C. Y. Wen, X. D. Tian, T. H. Long, and W. Yuan, "Numerical simulation of local wall heating and cooling effect on the stability of a hypersonic boundary layer," *Int. J. Heat Mass Transfer* **121**, 986–998 (2018).
- <sup>37</sup>R. Zhao, T. Liu, C. Y. Wen, J. Zhu, and L. Cheng, "Theoretical modeling and optimization of porous coating for hypersonic laminar flow control," *AIAA J.* **56**, 2942–2946 (2018).
- <sup>38</sup>B. T. Chu, "On the energy transfer to small disturbances in fluid flow (part I)," *Acta Mech.* **1**, 215–234 (1965).